Revealing a High Water Abundance in the Upper Mesosphere of Mars With ACS Onboard TGO

Denis A. Belyaev, Anna A. Fedorova, Alexander Trokhimovskiy, Juan Alday,
Franck Montmessin, Oleg I. Korablev, Franck Lefèvre, Andrey S. Patrakeev,
Kevin S. Olsen, Alexey V. Shakun

1

Revealing a High Water Abundance in the Upper Mesosphere of Mars with ACS onboard TGO

2
3

4 **Denis A. Belyaev[1], Anna A. Fedorova[1], Alexander Trokhimovskiy[1], Juan Alday[2], Franck**
5 **Montmessin[3], Oleg I. Korablev[1], Franck Lefèvre[3], Andrey S. Patrakeev[1], Kevin S. Olsen[2],**
6 **and Alexey V. Shakun[1]**

7 [1]Space Research Institute (IKI), Moscow, Russia.

8 [2]Department of Physics, University of Oxford, UK.

9 [3]LATMOS/CNRS, Paris, France.

10 Corresponding author: Denis Belyaev (dbelyaev@iki.rssi.ru)

11 **Key Points:**

12 • For the first time, water relative abundances are reported in a previously unexplored
13   altitude range: from 100 to 120 km

14 • Both the global dust storm (MY34) and the two perihelion seasons (MY34, 35) observed
15   reveal 10–50 parts of H_2O per million by volume at 100–120 km

16 • Contributions of a single GDS and perihelion into the H escape from Mars are nearly
17   equivalent, suggesting the repeatable seasonal effect dominates in the long term
18

Abstract

We present the first water vapor profiles encompassing the upper mesosphere of Mars, 100–120 km, far exceeding the maximum altitudes where remote sensing has been able to observe water to date. Our results are based on solar occultation measurements by Atmospheric Chemistry Suite (ACS) onboard the ExoMars Trace Gas Orbiter (TGO). The wavelength range observed (~2.7 μm) possesses strong CO_2 and H_2O absorption lines allowing sensitive temperature and density retrievals. We report the maximum H_2O mixing ratio varying from 10 to 50 ppmv at 100–120 km during the global dust storm of MY34 and around southern summer solstice of Martian Years (MY) 34 and 35. During other seasons water remains below 2-3 ppmv. The high values above 100 km establish a bridge between the regular water enrichment observed below (60-100 km) and the atomic hydrogen escaping from the exosphere.

Plain Language Summary

We report regular events of high abundances of the water vapor (H_2O) in the upper atmosphere of Mars (100–120 km). So far, any water enrichment has not been revealed by remote sensing at such high altitudes. Higher than 80 km, solar light breaks water vapor molecules into H and O atoms, which may reach the exosphere and escape the planet. When Mars is closer to the Sun (the perihelion season), the atmosphere's circulation intensifies, causing increased dust activity with global dust storms (GDS), occurring every 3–4 Mars years. We observed during the second halves of Martian years 34 and 35 (2018–2020), including one GDS and two perihelion seasons. We report that the maximum water relative abundance reaches 10–50 parts per million in volume (ppmv) at 100-120 km during the GDS and every perihelion season. These high values indicate that the Martian atmosphere above 100 km regularly hosts large amounts of water, facilitating the long-term escape of water from the planet.

1 Introduction

The vertical distribution of water vapor (H_2O) on Mars is an indicator of the intricate coupling of distinct phenomena: temperature variations, cloud formation, sublimation, turbulent and convective mixing, etc. H_2O is usually expected to be confined below the hygropause, which is the level where the saturation condition is met and where water ice clouds may form, as occurs on Earth. For the first time, this layer was established on Mars by ground-based microwave soundings of Clancy et al. (1996) with a saturation level between 10–20 km around the aphelion, i.e., Solar Longitudes (L_S) 70°, and 40–60 km around perihelion (L_S 250°). In parallel, Rodin et al. (1997) reported water vapor profiles retrieved from the solar occultations made by Auguste on Phobos-2 in 1989. The existence of a hygropause at 30–35 km (with a mixing ratio of 3 ppm) in the northern spring (L_S=0°–20°) near the equator was claimed. The first climatology of water vapor profiles was derived from SPICAM-IR solar occultations on Mars Express (MEx) (Fedorova et al., 2009; 2018; 2021; Maltagliati et al., 2013), covering eight Martian years. The hygropause level was found to vary from 40 to 80 km depending on season, latitude, and dust events.

The observation of large amounts of water vapor in and above the middle atmosphere (>40 km) was accompanied by the discovery of fast variations of the hydrogen corona over several weeks (Chaffin et al., 2014; Clarke et al., 2014). This variability suggested a new paradigm in the perception of how water escapes from Mars (Chaffin et al., 2017). So far, water escape was thought to be controlled by a slow process involving H_2, formed from the catalytic

62 recombination of carbon dioxide with odd hydrogen (McElroy and Donahue, 1972;
63 Krasnopolsky, 2002). The non-condensable H_2 can overcome the hygropause and reach the
64 mesosphere (80–120 km) transported by turbulent mixing or circulation. There it can dissociate
65 and release H atoms that will escape the planet once above the exobase.

66   Long-term observations revealed that water vapor transport from the troposphere into the
67 lower mesosphere of Mars occurs during major dust storms. In particular, a significant H_2O
68 enhancement in the middle atmosphere was observed during the global dust storm (GDS) in
69 2007 (MY28) with a rise of the hygropause altitude to >60 km (Fedorova et al., 2018; Heavens et
70 al., 2018). Sensitive solar occultation measurements by NOMAD and ACS NIR instruments
71 onboard the ExoMars Trace Gas Orbiter (TGO) showed water reaching 80–100 km (Aoki et al.,
72 2019; Fedorova et al., 2020) during two storms in 2018-2019 (the global one at L_S 190°–220°
73 and the regional one at L_S 330° in MY34; Montabone et al., 2020). Fedorova et al. (2020)
74 revealed the water supersaturation at 70–90 km even in the presence of H_2O ice clouds not only
75 during the GDS but also near the Southern summer solstice ($L_S \sim 270^o$) when water reached 90-
76 100 km as well. Altogether, these studies promote a new mechanism for controlling H_2O escape
77 through direct delivery to above 80 km and further photodissociation (Chaffin et al., 2017;
78 Krasnopolsky et al., 2019). The only general circulation model describes an upward water flux
79 into the thermosphere (>120 km) for the GDS scenario (Shaposhnikov et al., 2019). They predict
80 high water volume mixing ratio (VMR) values: ~100 ppm at 100 km and ~200 ppm at 150 km
81 for the southern middle latitudes.

82   The discussion regarding a relative contribution of perihelion or GDS to the mesospheric
83 water enrichment was recently fed by SPICAM/MEx long-term observations covering Martian
84 Years 28 through 35. Here, Fedorova et al. (2021) claimed a regular rise of water abundance up
85 to 80–90 km in perihelion, which is compatible with GDS quantities. The new ACS/TGO dataset
86 confirms those conclusions for altitudes below 100 km in MY34–MY35 (Fedorova et al. 2020,
87 Alday et al., 2021). In parallel, during the perihelion season, the D/H ratio in water decreases
88 with altitude from 4–6 times SMOW (Standard Mean Ocean Water) in the lower atmosphere to
89 2–3 times in the middle one (50-70 km) as measured by ACS MIR (Alday et al., 2021) and
90 NOMAD (Villanueva et al., 2021) spectrometers. Alday et al. (2021) show that ultraviolet H_2O
91 photolysis dominates the production of H relative to D atoms in the upper atmosphere.

92   From above, ion chemistry in the thermosphere has been characterized by the NGIMS
93 mass-spectrometer on MAVEN (Benna et al., 2015) and interpreted by the ionospheric model of
94 Fox et al. (2015). Using NGIMS data, Stone et al. (2020) measured H_2O ion concentrations
95 around ~150 km for the 2014–2018 period (MY32–MY34). With the help of the model by Fox et
96 al., the relative abundance of water at this altitude on the dayside was found to vary seasonally
97 from 2 to 5 ppm. Several enhanced dusty episodes disrupt this seasonal signal: 7–9 ppm during
98 the regional storm of MY32, 10–20 ppm in the southern summer of MY33, and up to 60 ppm in
99 the GDS of MY34. Stone et al. (2020) concluded that water transport into the ionosphere and its
100 destruction are the main mechanisms in the overall hydrogen escape from Mars.

101   We used the data of the middle infrared spectrometer of the Atmospheric Chemistry Suite
102 (ACS MIR) onboard the ExoMars TGO, which measures water vapor VMR and atmospheric
103 density in a wide range of altitudes, from the troposphere to the lower thermosphere, using the
104 strong absorption bands of H_2O and CO_2 around 2.66–2.70 μm. A high spectral resolution and a
105 good signal-to-noise ratio of ACS MIR allows the measurements of water profiles up to 120 km,
106 the altitude unreachable for the ACS NIR, and SPICAM spectrometers, sensing the 1.38 μm

107 absorption band (Fedorova et al., 2020; 2021). The strong H_2O absorption around 2.6 μm is also
108 used by NOMAD, yielding water profiles up to ~90 km (Aoki et al., 2019; Villanueva et al.,
109 2021).

110 Here we report the first water vapor abundance measurements in the upper mesosphere
111 (up to 120 km) of Mars. The goal of our paper is to compare the mesospheric water behavior
112 between the second halves of MY34 and MY35 when the high H_2O content is observed. We aim
113 to clarify the dominant role of H_2O delivery to the upper mesosphere: either it belongs to
114 sporadic dust events (GDS or a strong regional storm) or it also occurs regularly, every martian
115 year, around Southern summer solstice. For that, we analyze seasonal and latitudinal variations
116 of H_2O VMR vertical profiles retrieved from the ACS MIR solar occultation experiment.

117 **2 Measurements and dataset overview**

118 2.1 ACS MIR spectroscopy and retrievals

119 ACS MIR, a solar occultation cross-dispersion echelle spectrometer, records spectra from
120 a set of adjacent diffraction orders (from 10 to 20 per occultation) projected onto a 2D detector
121 array (Korablev et al., 2018). To retrieve high altitude water vapor abundances together with the
122 atmospheric temperature and pressure, we use MIR spectra from the diffraction order #223. They
123 cover a narrow wavelength interval of 2.66–2.68 μm (3733–3753 cm^{-1}), including a part of the
124 2.7-μm CO_2 absorption band and a few strong H_2O lines near 2.66 μm (Fig. 1a, 1b, Fig. S1). The
125 instrument's spectral resolution is ~0.15 cm^{-1}, while the signal-to-noise ratio ranges from 2,000
126 to 4,000, which provides high sensitivity for detections in the upper atmosphere where
127 atmospheric constituents are low. Temperature (Fig. 1c) is retrieved by fitting a synthetic model
128 to the CO_2 rotational band taking advantage of its temperature dependence under the assumption
129 of hydrostatic equilibrium. This procedure was applied iteratively, with feedback of the retrieved
130 temperature to the model. The temperature measurements were then validated against those
131 made by MIR near the 2.6 μm CO_2 band (Alday et al., 2019) and by ACS NIR around the 1.58
132 μm band (Fedorova et al., 2020). As a result, one occultation session allows us to simultaneously
133 retrieve profiles of pressure and temperature (from CO_2 absorption bands) and the H_2O number
134 density (Fig. 2c). The water abundance can then be expressed relative to the total atmospheric
135 density, that is, in VMR (in ppmv). Specific details of the algorithms pertaining to this work can
136 be found in the Supporting Information.

137 The dataset analyzed here consists of a series of transmission spectra obtained during a
138 solar occultation while the line of sight of the instrument progressively penetrates from the upper
139 into deeper layers of the atmosphere, or vice versa (see examples in Fig. 1a, 1b). The
140 transmission is determined as the solar spectrum ratio measured through the atmosphere to the
141 reference one, taken from the data above a tangential height of 200 km. This altitude level is
142 negligibly attenuated by the atmosphere even within the very strong CO_2 band system at 2.7 μm.
143 The typical integration time is 2 seconds that provides an altitude resolution ranging from 0.5 to
144 2.5 km, depending on the occultation duration. It gives sufficiently fine vertical sampling for an
145 atmosphere whose scale height ranges from 5 to 10 km depending on temperature. The ACS
146 MIR field of view projected at the limb is estimated to be around 1-3 km in altitude equivalent.
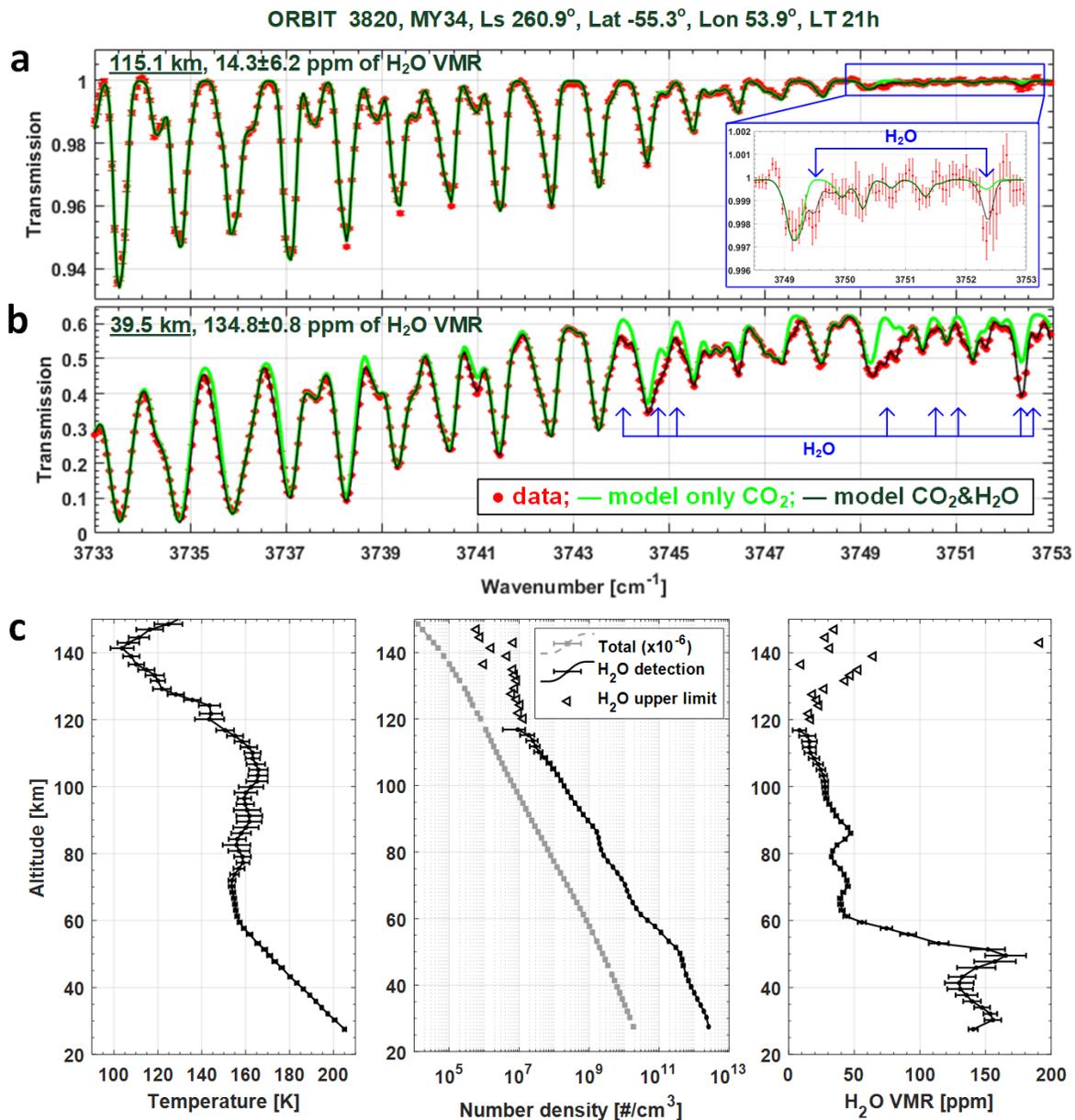
Figure 1. Example ACS MIR spectra and profiles of the retrieved quantities. Measured transmission spectra (red) at tangent altitudes of 115.1 km (**a**) and 39.5 km (**b**) are compared with the best-fit models, including both CO_2 and H_2O absorptions (black), and only CO_2 absorption (green). Blue arrows indicate water absorption lines. Zoom in (**a**) shows a part with the strongest H_2O absorption detected at 115 km. (**c**) Retrieved vertical profiles of temperature (left), number densities (center), and H_2O volume mixing ratio (VMR) (right). Black triangles mark H_2O upper limits (see Supporting Information for the description of uncertainties).

2.2 Data selection

To reveal the upper mesospheric water we focused on the second halves of MY34 and MY35, which correspond to ACS MIR observations from May 2018 to March 2019 and from April 2020 to January 2021. The selected dataset comprises 187 occultation sessions in the

159 Northern Hemisphere and 156 sessions in the Southern Hemisphere, encompassing seasonal
160 periods from L_S 180° to 355° in MY34 and from L_S 185° to 356° in MY35 (Fig. 2a). Figure 2a
161 shows the latitude coverage with the corresponding aerosol activity, which was defined for each
162 occultation as an altitude level where the slant opacity equals 0.3 (~0.75 of the atmospheric
163 transmittance in the continuum). Measurements in the Northern Hemisphere occurred mostly in
164 the mid-latitude range, which is between 40°N and 70°N. In the South, occultations before,
165 during the GDS (L_S<230°), and around the regional storm of MY34 (L_S 320°–330°) were
166 performed close to the polar region (60°S–90°S), while perihelion observations (L_S 270°) were
167 made in mid-latitudes. Only a few sessions occurred in the equatorial region at L_S~240° and
168 L_S~300° of MY34 and at L_S~210° and L_S~280° of MY35. These observations are accompanied
169 by a higher aerosol loading than those, which are close to the Poles (Fig. 2a). The overall map of
170 the MY34 dust climatology can be found in (Montabone et al., 2020).

171 **3 Seasonal variation of altitude profiles**

172 Observations in the second half of MY34 and MY35 uncover events, which drastically
173 perturbed the temperature and water vapor vertical distributions. The peculiar pattern to compare
174 with is the MY34 GDS and perihelion periods in MY34 versus MY35, which had no GDS but a
175 regular dust activity in its second half. The seasonal variation of the processed altitude profiles is
176 presented in Figure 2(b,c). We binned the profiles into intervals of 2° in solar longitude (L_S) and
177 2 km in altitude. Depending on the L_S and altitude sampling, the value in each bin is calculated
178 as the weighted mean of one to five individual points. We excluded all points with uncertainties
179 exceeding 20 K in temperature and 1-sigma in the H_2O mixing ratio. The second rejection
180 criterion corresponds to the detection limit (~10^7 cm^{-3}) of water number density (see in Fig. 1c)
181 that defines the seasonal variations of the uppermost detectable points in Figure 2c.

182 We observe temperature (Fig. 2b) and H_2O (Fig. 2c) peaking in the middle atmosphere
183 (40–80 km) during the GDS of MY34, L_S 190°–220°, and an additional smaller peak at L_S 320°–
184 330°, corresponding to a regional storm. Moreover, the rise of water vapor to higher altitudes, up
185 to the mesopause at 110–130 km where temperature encounters a minimum, is observed during
186 two perihelion intervals (L_S 250°–290°) of MY34 and MY35. Here, the Southern summer (Fig.
187 2c, right panel) is accompanied by a more humid mesosphere (40–60 ppm of H_2O) than the
188 Northern Winter (Fig. 2c, left panel) where the mean mesospheric water reaches 20–30 ppmv on
189 average between 80 and 120 km. On the contrary, out of the perihelion peak or dust events, i.e.
190 for the selected data at the beginning of the MY34 GDS and at the very end of MY 34, 35, water
191 content above 80 km never exceeds 2-3 ppmv.
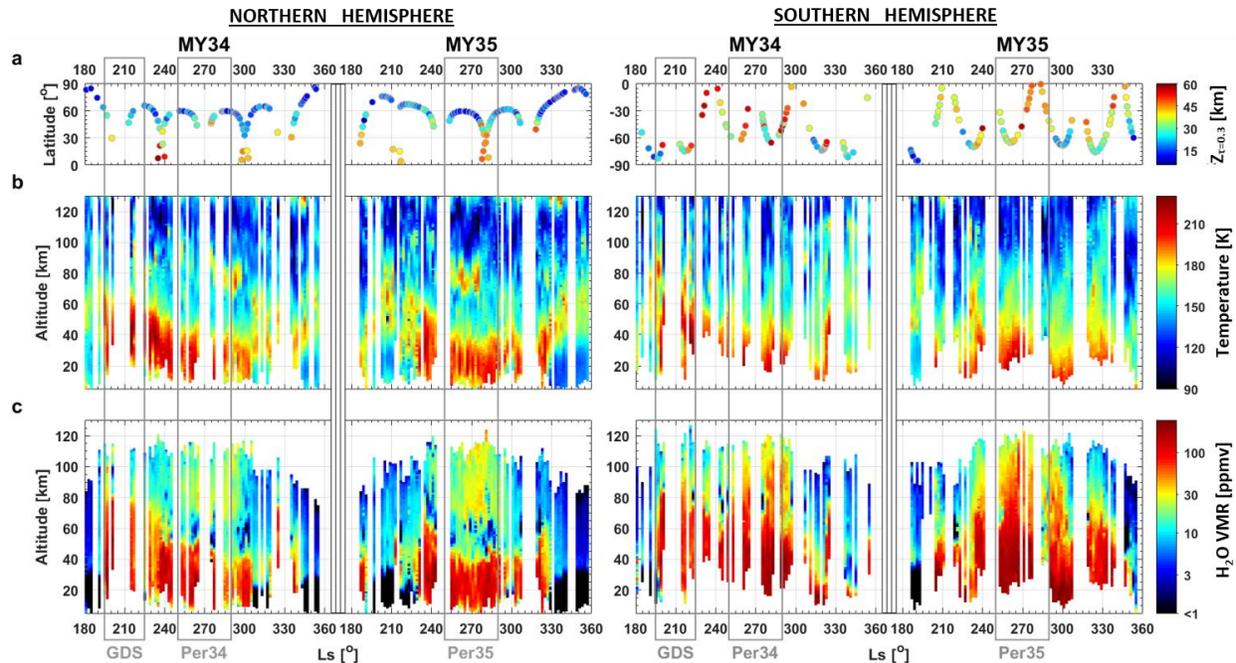
Figure 2. Seasonal map of atmospheric temperature and H_2O mixing ratio during the second half of MY34 and MY35. The data are plotted in function of L_S and altitude for the Northern (left) and the Southern (right) hemispheres. (**a**) Latitudinal distribution of the ACS-MIR solar occultations, depending on an altitude level where the aerosol slant opacity (τ) equals 0.3. (**b**) Temperature. (**c**) Volume mixing ratio (VMR) of water vapor. Grey frames outline time intervals of the global dust storm (GDS) in MY34 and the two perihelions in MY34 (Per34) and MY35 (Per35).

4 H_2O variations around perihelion

To quantify seasonal trends of water content in the mesosphere, we selected three altitude layers corresponding to 80 km, 100 km, and 110–120 km. The first layer, which corresponds to the lower mesosphere, is accessible in all profiles (Fig. 2c) when the vapor concentration exceeds the detection limit of ~10^7 cm^{-3}, even in low water loading periods. A value of H_2O VMR at 80 km could be derived in every individual altitude profile when interpolating between adjacent points below and above this level. The water content at 100 km was found similarly, though based on a smaller number of profiles. Water at 110–120 km, in the upper mesosphere, shows up only in stormy periods and around perihelion (Fig. 2c).

Observed variations during perihelion for the three selected levels are presented in Figure 3 for both Martian Years. The number of MIR observations at Position #4 is low during the stormy events of MY34. Nevertheless, a comparison with MY35 reveals a significant excess of H_2O mixing ratio during the GDS: by a factor of 6–8 at 80 km (Fig. 3c) and by a factor of 3–5 at 100-120 km from L_S 190° to 220° (Fig. 3a, 3b). A surge at L_S 320°–330° reveals the effect of the regional dust storm of MY34, which delivers far less water into the mesosphere than the GDS. Around the perihelion, L_S=240°–300° water behaves almost identical between MY34 and MY35. For both Martian Years, the maximum H_2O mixing ratio was observed near the Southern summer solstice (L_S~270°), reaching values of 40–80 ppm at 80 km, 30–60 ppm at 100 km, and 20–50 ppm at 110–120 km. In the Northern winter solstice, it varied from 20 to 40 ppm at all

219   levels, 80 through 120 km. We compare our results at 80 km with the corresponding ACS NIR
220   dataset derived from the MY34 profiles of Fedorova et al. (2020). The NIR dataset is five times
221   denser than used in the present work, and it observed the H_2O variations in greater detail,
222   especially during the dust events of MY34.
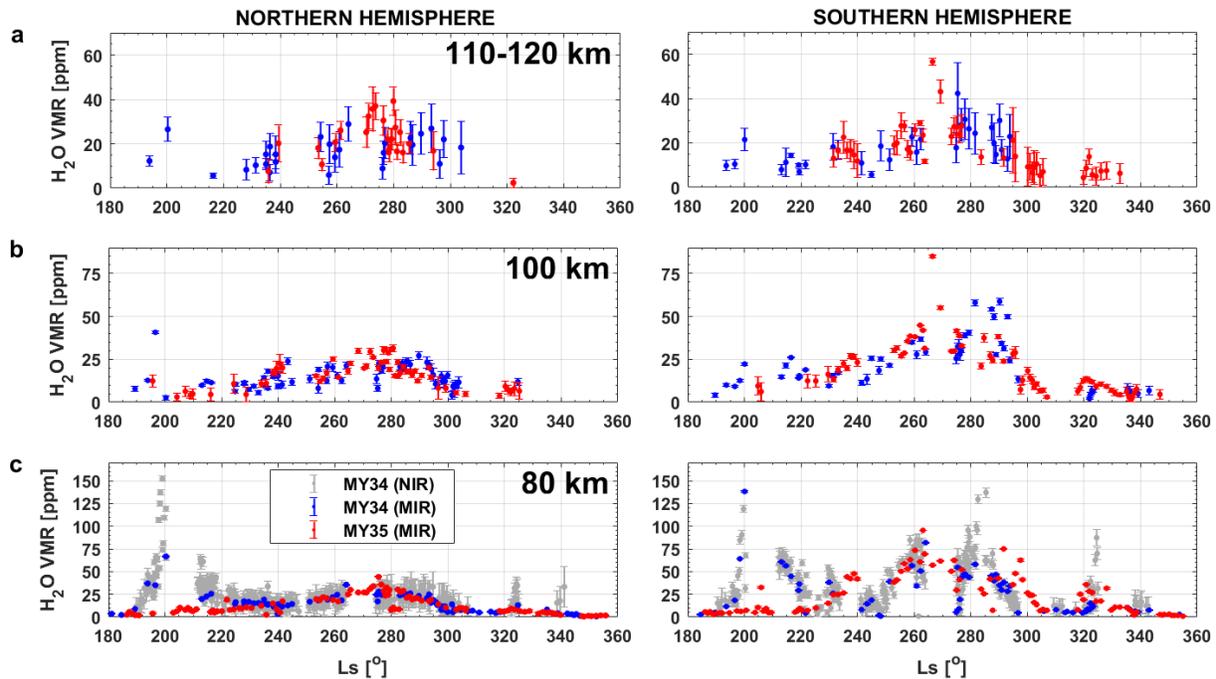
223

224   **Figure 3**. Seasonal trends of H_2O volume mixing ratio (VMR) at three altitude levels, 80, 100,
225   120 km. The season is the second half of MY34 (in blue) and of MY35 (in red). Each point
226   corresponds to an individual vertical profile: weighted mean value obtained in between 110-120
227   km (**a**), and interpolated value for the levels of 100 km (**b**) and 80 km (**c**). Data at 80 km in grey
228   (**c**) are taken from the ACS NIR profiles (Fedorova et al., 2020).

4 Discussion and Conclusions

230   For the first time, we report observations of H_2O relative abundances in a previously
231   unexplored altitude range (from 100 to 120 km). There we find 10–30 ppm of water vapor during
232   the MY34 GDS and 20–50 ppm around the perihelion point (L_S=250°–290°) of MY34 and
233   MY35 in both hemispheres. Our stormy retrievals at 100–120 km are of the same order of
234   magnitude as MAVEN NGIMS results reported by Stone et al. (2020) at ~150 km. Surprisingly,
235   NGIMS water relative abundances reveal a mission-wise maximum of H_2O at 150 km during the
236   MY34 GDS, whereas we repeatedly observe the annual maximum around the Southern summer
237   solstice both in MY34 and MY35.

238   NGIMS measures ions from which neutral H_2O VMRs at 150 km were derived and
239   injected into a 1D photochemical model. The model was adjusted to reproduce the H_2O
240   abundance at 150 km inferred from the $[H_2O^+]$ ions measured by NGIMS under two scenarios:
241   low water, corresponding to 2 ppm prescribed at 80 km in a non-GDS case; and high water, of 40
242   ppm in a GDS case (Stone et al., 2020; as corrected in March 2021). Notably, all the solar
243   occultation observations performed by TGO and MEX to date (Fedorova et al., 2018, 2020,
244   2021; Aoki et al., 2019; Villanueva et al., 2021), including the present dataset (Fig. 3a), report

245 even higher water vapor VMRs, of 50–80 ppm during the GDS. Stone et al. (2020) indicate a
246 systematic uncertainty of 69% on their neutral H_2O inference, which brings MAVEN, TGO, and
247 MEX values to an agreement within error bars.

248   It is important to consider how ACS's high altitude water vapor abundances combine
249 with photolysis since this process has been hypothesized to be essential, if not the dominant,
250 source for the H atoms observed in the exosphere (Chaffin et al., 2017). The conclusion of Stone
251 et al. (2020) insists on the GDS's predominance and related ion chemistry in the H atoms'
252 production. Our observations suggest that while the GDS period corresponds to the maximum of
253 water abundance at 80 km, H_2O at 120 km peaks only later, at the Southern summer solstice,
254 when it is twice as large as during the GDS. This enhanced solstice maximum suggests that
255 relative water abundance declines more rapidly above 80 km during the GDS than after, during
256 perihelion (Fig. 4).

257
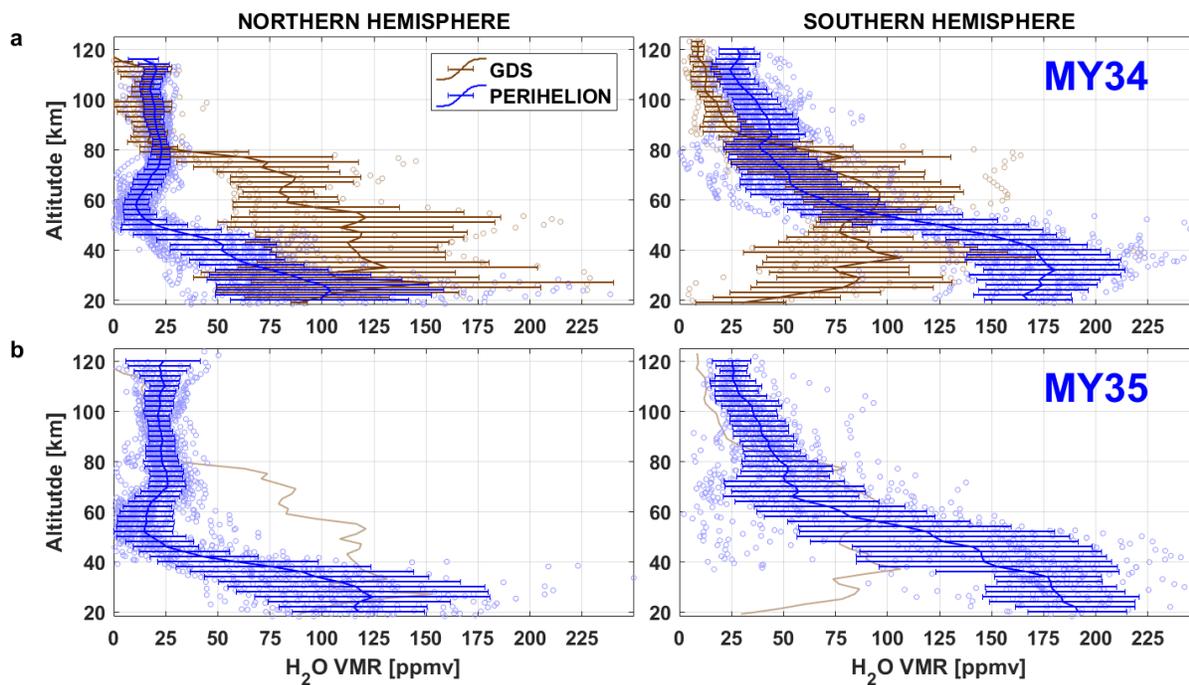
Figure 4. Altitude profiles of average H_2O volume mixing ratio (VMR) during the GDS (MY
259 34) and the perihelion season (MY 34, 35). The dataset used includes all ACS MIR observations
260 highlighted in Fig. 2: GDS of MY34 (L_S=195°–220°), brown average curve, and individual MIR
261 detections; the bin around the perihelion point (L_S=250°–295°) (blue). Upper panels: MY34 (**a**);
262 lower panels: MY35 (**b**). The left and right panels are for the Northern and Southern
263 hemispheres. Averaged profiles are presented with 1-sigma dispersion over 2-km altitude bins.
264 The GDS curves are also indicated for MY35 to facilitate comparison.

265   In Figure 4, we combined altitude profiles from GDS-only (L_S 195°–220°) and perihelion
266 (L_S 250°–295°) intervals to compare averaged vertical trends between them and to estimate an
267 integral escape flux of the atomic hydrogen in each case. For that, we applied the model of
268 Chaffin et al. (2017), which predicts the atmospheric escape rate depending on the water
269 injection into different altitudes (see Figure 3 of their paper). Our rough calculations show that
270 the H escape flux is about 5.7×10^9 cm^{-1}s^{-1} during GDS for both hemispheres, while around
271 perihelion point it is 4.0×10^9 cm^{-1}s^{-1} for the Northern Hemisphere and 6.0×10^9 cm^{-1}s^{-1} for the

272 Southern one in both Martian Years. These values were derived when integrating the flux over
273 altitudes from 20 to 120 km and in time intervals of 25 sols for GDS (L_S 195°–220°) and 45 sols
274 for perihelion (L_S 250°–295°). Thus, we claim nearly equivalent contributions from a single
275 GDS and the perihelion period into the hydrogen escape by the high water enrichment in the
276 middle/upper atmosphere. Fedorova et al. (2021) come to a similar conclusion based on
277 SPICAM/MEx water profiles up to 80 km. A GDS occurs every 3–4 martian years on average
278 (Zurek and Martin, 1993; Wang and Richardson, 2015), and the yearly perihelion contribution to
279 the hydrogen escape should prevail by a factor of ≥3.5. Moreover, the enhanced circulation and
280 heating of the atmosphere in perihelion driven by the hemispheric dichotomy of Mars
281 (Richardson and Wilson, 2002) might be, in the long term, a more robust climate phenomenon
282 rather than GDS, likely affected by changing obliquity of the planet (Laskar, 2004).

283   Overall, our results cannot be easily reconciled with water values inferred from NGIMS
284 ion measurements, suggesting the thermosphere hosts much more water during the GDS than
285 during the rest of the year. However, we note that the only time when Stone et al. (2020)
286 reported measurements around perihelion concerned the L_S interval between 240° and 265° of
287 MY33 (Figure 4 of Stone et al., 2020). It showed the same brutal trend as during the onset of the
288 MY34 GDS, with values far exceeding those reported for the regional dust storm of MY32, still
289 a factor of 3 smaller than during the GDS.

290   Our results remain in line with Fedorova et al. (2020, 2021) conclusion about the
291 perihelion season being the main conveyor of water to high altitudes on a long-term basis. A
292 bridge between the ACS measurements presented here and NGIMS measurements leaves room
293 for an additional or refined photochemical process that could link H_2O relative abundances at
294 120 km with those inferred from NGIMS at 150 km. Both measurements bring unique
295 constraints in our attempt to understand how the water in the lower atmosphere connects with the
296 escaping hydrogen in the exosphere, an essential step before extrapolating the water escape back
297 in time safely.

Acknowledgments, Samples, and Data

References

309 Alday, J., Wilson C. F., Irwin, P. G. J., Olsen, K. S., Baggio, L., Montmessin, F., et al. (2019).
310   Oxygen isotopic ratios in Martian water vapour observed by ACS MIR on board the
311   ExoMars Trace Gas Orbiter. *Astronomy and Astrophysics*, *630*, A91. doi:10.1051/0004-
312   6361/201936234.

313   Alday, J., Trokhimovskiy, A ., Irwin, P. G. J., Wilson, C. F., Montmessin, F., Lefèvre, F., et al.
314   (2021). Photolysis controls the isotopic composition of water products escaping Mars'
315   atmosphere. *Nature Astronomy* (revised version).

316   Aoki, S., Vandaele, A. C., Daerden, F., Villanueva, G. L., Liuzzi, G., Thomas, I. R., et al. (2019).
317   Water Vapor Vertical Profiles on Mars in Dust Storms Observed by TGO/NOMAD.
318   *Journal of Geophysical Research: Planets*, *124*(12), 3482-3497.
319   doi:10.1029/2019je006109.

320   Benna, M., Mahaffy, P. R., Grebowsky, J. M., Fox, J. L., Yelle, R. V., & Jakosky, B. M. (2015).
321   First measurements of composition and dynamics of the Martian ionosphere by
322   MAVEN's Neutral Gas and Ion Mass Spectrometer. *Geophysical Research Letters*, *42*,
323   8958–8965, doi:10.1002/2015GL066146.

324   Chaffin, M., Deighan, J., Schneider, N., & Stewart, A. (2017). Elevated atmospheric escape of
325   atomic hydrogen from Mars induced by high-altitude water. Nature Geoscience, 10(3),
326   174. doi:10.1038/ngeo2887.

327   Clancy, R. T., Grossman, A. W., Wolff, M. J., James, P. B., Rudy, D. J., Billawala, Y. N., et al.
328   (1996). Water vapor saturation at low altitudes around Mars aphelion: A key to Mars
329   climate? *Icarus*, *122*(1), 36-62. doi:10.1006/icar.1996.0108.

330   Fedorova, A., Bertaux, J.-L., Betsis, D., Montmessin, F., Korablev, O., Maltagliati, L., & Clarke,
331   J. (2018). Water vapor in the middle atmosphere of Mars during the 2007 global dust
332   storm. Icarus, 300, 440–457.

333   Fedorova, A. A., Montmessin, F., Korablev, O., Luginin, M., Trokhimovskiy, A., Belyaev, D.
334   A., et al. (2020). Stormy water on Mars: The distribution and saturation of atmospheric
335   water during the dusty season. *Science*, *367*(6475), 297-300.
336   doi:10.1126/science.aay9522.

337   Fedorova, A., Montmessin, F., Korablev, O., Lefèvre, F., Trokhimovskiy, A., & Bertaux, J. L.
338   (2021). Multi-annual monitoring of the water vapor vertical distribution on Mars by
339   SPICAM on Mars Express. *Journal of Geophysical Research: Planets*, *126*,
340   e2020JE006616. doi:10.1029/2020JE006616.

341   Fox, J. L., Benna, M., Mahaffy, P. R., & Jakosky B. M. (2015). Water and water ions in the
342   Martian thermosphere/ionosphere. *Geophysical Research Letters*, *42*, 8977–8985,
343   doi:10.1002/2015GL065465.

344   Gamache, R. R., Farese, M., & Renaud, C. L. (2016). A spectral line list for water isotopologues
345   in the 1100–4100 cm-1 region for application to CO_2-rich planetary atmospheres. *Journal*
346   *of Molecular Spectroscopy*, *326*, 144-150. doi:10.1016/j.jms.2015.09.001.

347   Gordon, I. E., Rothman, L. S., Hill, C., Kochanov, R. V., Tan, Y., Bernath, P. F., et al. (2017).
348   The HITRAN2016 molecular spectroscopic database. *Journal of Quantum Spectroscopy*
349   *and Radiative Transfer*, *203*, 3–69. doi:10.1016/j.jqsrt.2017.06.038.

350   Heavens, N. G., Kleinböhl, A., Chaffin, M. S., Halekas, J. S., Kass, D. M., Hayne, P. O., et al.
351   (2018). Hydrogen escape from Mars enhanced by deep convection in dust storms. *Nature*
352   *Astronomy*, *2*(2), 126-132. doi:10.1038/s41550-017-0353-4

353 Jakosky, B. M. (1985). The seasonal cycle of water on Mars. *Space Science Review*, *41*, 131–
354   200. doi:10.1007/BF00241348

355 Korablev, O. I., Montmessin, F., Trokhimovskiy, A., Fedorova, A. A., Shakun, A. V., Grigoriev,
356   A. V., et al. (2018). The Atmospheric Chemistry Suite (ACS) of Three Spectrometers for
357   the ExoMars 2016 Trace Gas Orbiter. *Space Science Review*, *214*(1).
358   doi:10.1007/s11214-017-0437-6

359 Krasnopolsky, V. A. (2002). Mars' upper atmosphere and ionosphere at low, medium, and high
360   solar activities: implications for evolution of water. *Journal of Geophysical Research*,
361   *107*(E12), 5128. doi:10.1029/2001JE001809.

362 Krasnopolsky, V. A. (2015). Variations of the HDO/H2O ratio in the martian atmosphere and
363   loss of water from Mars. *Icarus*, *257*, 377–386. doi:10.1016/j.icarus.2015.05.021.

364 Krasnopolsky, V. A. (2019). Photochemistry of water in the martian thermosphere and its effect
365   on hydrogen escape. *Icarus*, *321*, 62–70. doi:10.1016/j.icarus.2018.10.033.

366 Laskar, J., Correia, A.C.M., Gastineau, M., Joutel, F., Levrard, B., Robutel, P. (2004). Long term
367   evolution and chaotic diffusion of the insolation quantities of Mars. *Icarus*, *170*(2), 343-
368   364. doi:10.1016/j.icarus.2004.04.005.

369 Malathy Devi, V., Benner, D. C., Sung, K., Crawford, T. J., Gamache, R. R., Renaudc, C. L., et
370   al. (2017). Line parameters for CO_2- and self-broadening in the v3 band of $HD^{16}O$.
371   *Jouranal of Quantum Spectroscopy and Radiative Transfer*, *203*, 158–174.
372   doi:10.1016/j.jqsrt.2017.02.020.

373 Maltagliati, L., Montmessin, F., Korablev, O., Fedorova, A., Forget, F., Määttänen, A., Lefèvre,
374   F., & Bertaux, J.-L. (2013). Annual survey of water vapor vertical distribution and water–
375   aerosol coupling in the martian atmosphere observed by SPICAM/MEx solar
376   occultations. *Icarus*, *223*, 942–962. doi:10.1016/j.icarus.2012.12.012.

377 Marquardt, D. (1963). An Algorithm for Least-Squares Estimation of Nonlinear Parameters".
378   SIAM. *Journal on Applied Mathematics*, *11*(2), 431–441. doi:10.1137/0111030.

379 Millour, E., Forget, F., Spiga, A., Vals, M., Zakharov, V., Montabone, L., et al. (2018). *The Mars*
380   *Climate Database (version 5.3)*. Paper presented at the Mars Science Workshop "From
381   Mars Express to ExoMars", held 27-28 February 2018 at ESAC, Madrid, Spain, id.68.
382   https://www.cosmos.esa.int/web/mars-science-workshop-2018.

383 McElroy, M. B., & Donahue, T. M. (1972). Stability of the Martian atmosphere. *Science*,
384   *177*(4053), 986-8 986. doi:10.1126/science.177.4053.986.

385 Montabone, L., Spiga, A., Kass, D. M., Kleinböhl, A., Forget, F., & Millour, E. (2020). Martian
386   Year 34 column dust climatology from Mars Climate Sounder observations:
387   Reconstructed maps and model simulations. *Journal of Geophysical Research: Planets*,
388   *125*(8), e06111. doi:10.1029/2019JE006111.

389 Owen, T., Maillard, J. P., de Bergh, C., & Lutz, B. L. (1988). Deuterium on Mars: The
390   abundance of HDO and the value of D/H. *Science*, *240*, 1767–1770.
391   doi:10.1126/science.240.4860.1767.

392 Richardson, M. I., & Wilson, R. J. (2002). Investigation of the nature and stability of the Martian
393   seasonal water cycle with a general circulation model. *Journal of Geophysical Research*,
394   *107*(E5), 5031, doi:10.1029/2001JE001536.

395 Rodin, A. V., Korablev, O. I., & Moroz, V. I. (1997). Vertical distribution of water in the near-
396   equatorial troposphere of Mars: water vapor and clouds. *Icarus*, *125*(1), 212-229.
397   doi:10.1006/icar.1996.5602.

398 Shaposhnikov, D. S., Medvedev, A. S., Rodin, A. V., & Hartogh, P. (2019). Seasonal water
399   "pump" in the atmosphere of mars: Vertical transport to the thermosphere. *Geophysical
400   Research Letters*, *46*, 4161–4169. doi:10.1029/2019GL082839.

401 Stone, W., Yelle, R. V., Benna, M., Lo, D. Y., Elrod, M. K., & Mahaffy P. R. (2020). Hydrogen
402   escape from Mars is driven by seasonal and dust storm transport of water. *Science*,
403   *370*(6518), 824–831. doi:10.1126/science.aba5229.

404 Villanueva, G. L., Liuzzi, G., Crismani, M. M. J., Aoki, S., Vandaele, A. C., et al. (2021). Water
405   heavily fractionated as it ascends on Mars as revealed by ExoMars/NOMAD. *Science
406   Advances, 7*(7), eabc8843. doi:10.1126/sciadv.abc8843.

407 Wang, H., & Richardson, M. I. (2015). The origin, evolution, and trajectory of large dust storms
408   on Mars during Mars years 24-30 (1999-2011). *Icarus*, *251*, 112-127.
409   doi:10.1016/j.icarus.2013.10.033.

410 Zurek, R. W. & Martin, L. J. (1993). Interannual variability of planet-encircling dust storms on
411   Mars. *Journal of Geophysical Research*, *98*(E2), 3247-3259. doi:10.1029/92JE02936.